Investigation on shape deviation of horizontal interior circular channels fabricated by laser powder bed fusion

Feng, Shaochuan; Chen, Shijie ; Kamat, Amar M; Zhang, Ru ; Huang, Mingji; Hu, Liangcai

Link to publication in University of Groningen/UMCG research database
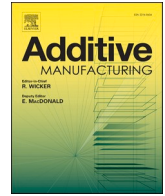
Investigation on shape deviation of horizontal interior circular channels fabricated by laser powder bed fusion

Shaochuan Feng [a],[*], Shijie Chen [a], Amar M. Kamat [b], Ru Zhang [c], Mingji Huang [a], Liangcai Hu [d]

[a] School of Mechanical Engineering, University of Science and Technology Beijing, Beijing 100083, China
[b] Department of Advanced Production Engineering, Engineering and Technology Institute Groningen, Faculty of Science and Engineering, University of Groningen, Nijenborgh 4, 9747 AG Groningen, the Netherlands
[c] Center for Advanced Jet Engineering Technologies (CaJET), Key Laboratory of High-Efficiency and Clean Mechanical Manufacture (Ministry of Education), National Demonstration Center for Experimental Mechanical Engineering Education, School of Mechanical Engineering, Shandong University, Jinan 250061, China
[d] The Fourth Research and Design Engineering Corporation of CNNC, Shijiazhuang 050021, China

ARTICLE INFO

ABSTRACT

The fabrication of horizontal interior circular channels poses some unique challenges to the laser powder bed fusion (L-PBF) process. The engineering challenge is to be able to print horizontal interior channels using L-PBF without using support structures, while the scientific challenge is to predict the shape deviation in the horizontal channel. This paper studies the geometric fidelity (roundness and shape deviation) of L-PBF printed horizontal interior circular channels (diameters $1-3$ mm) by developing experiment-based regression models and a preliminary computational fluid dynamics (CFD) simulation model. The roundness error is found to be affected by the shape/size of the melt pool, thermal stresses, beam offset, and the slicing algorithm. It is recommended that to decrease the roundness error, in addition to choosing a proper beam offset, the width/depth of the melt pool should be minimized by minimizing the volumetric energy density (smaller laser power or higher scanning speed). Shape deviation in overhanging structures is determined by the thermo-mechanical driven molten flow in the melt pool. Hanging structures with irregular profiles (dross) are formed due to the sinking of the melt pool on an unconsolidated powder bed under the effect of gravity, surface tension, and poor thermal conductivity. (Partially) unmelted powder randomly adheres to the edges of the melt pool enlarging the hanging structure and roughening the profile. Small laser power or large scanning speed benefits reducing the roundness error and hang-diameter ratio. 0° or 45° rotational linear scanning strategy can be selected for minimizing the roundness error or the hang-diameter ratio, respectively.

1. Introduction

The advances in additive manufacturing (AM) technology make it possible to fabricate freeform solids with complex internal structures directly from a computer-aided design (CAD) model without the need for specialized tooling. Laser powder bed fusion (L-PBF), also known as selective laser melting, is a type of AM for metallic materials in which metal powder is fused layer by layer; here, a high-energy focused laser beam melts the metal powder which subsequently solidifies to adhere onto the previously printed layers in the shape of the desired CAD model. The most popularly used alloys in L-PBF are stainless steel [1], Al-Si-10Mg [2], and Ti-6Al-4 V [3–5]. Studies on some other alloys such as Inconel [6], Ni-Ti [7] and WC-Co [8] have also been reported in the literature. Generally, post-printing machining processes, e.g. milling,

are employed as finishing techniques after L-PBF to improve the dimensional accuracy and surface quality of the printed parts.

A particularly interesting application for L-PBF is the fabrication of injection molds with conformal cooling channels that can improve cooling efficiencies and reduce residual stresses in the resulting plastic parts. A conformal cooling system is a series of interior channels with complex topological structures and cross-sections [9–11]. It plays a crucial role in a variety of industrial applications such as injection molding [12,13], blow molding [14], die casting [15], hot extrusion [16], hot embossing [17], and hot stamping [18]. Fabrication of conformal cooling systems is not possible using conventional manufacturing techniques such as drilling and is hence one of the attractive application cases for L-PBF. However, it poses some unique challenges to the L-PBF process. Some of the channels have to be printed horizontally and without support due to the difficulty in support

Nomenclature

D_d	designed inner diameter (m)
D_h	actual horizontal diameter (m)
D_l	actual vertical diameter (m)
E_R	roundness error
E_H	hang-diameter ratio
h	hatch distance (m)
L_h	hanging length (m)
P	laser power (W)
T	temperature (K)
t	layer thickness (m)
V_C	parameter value in terms of uniform coded unit
V_N	parameter value in terms of natural unit
V_0	value in terms of natural unit for parameter at Level 0
V_α	value in terms of natural unit for parameter at Level $+\alpha$
v	scanning speed (m/s)
α	coefficient for RSM design
Φ	volumetric energy density (J/m^3)

For regression models (Eqs. 4 and 5)

A	designed inner diameter (mm)
B	laser power (W)
C	scanning speed (mm/s)
F_1, F_2	coefficients

removal after printing. Moreover, the interior surfaces of these channels cannot be mechanically polished due to their structural limitations. In other words, high dimensional accuracy and surface quality must be ensured in the as-built channels when horizontally printing an interior channel without any supports.

The engineering challenge is thus to be able to print horizontal cooling channels using L-PBF without using support structures, while the scientific challenge is to predict (and compensate for, if possible) the shape deviation in the horizontal channel. This is a challenging task because of shortcomings inherent to the L-PBF process, such as shape deviations on overhanging regions caused by thermal stresses, and overheating damage on account of poor thermal conductivity of overhanging regions. Particularly, when horizontally printing a circular interior channel, two overhanging regions at the upper half of the channel are printed independently and finally welded together at the top of the channel. Excessive shape deviation can lead to part-recoater collisions or channel collapse causing build failure. Shape deviation for an internal channel can be divided into macro (thermal stress-induced warpage) and micro (surface roughness) deviation according to their length scales. A smaller interior channel (dimension $\sim 1-3$ mm) is more sensitive to micro shape deviations as compared to a larger channel. The L-PBF process physics involves a series of complex thermal, mechanical and fluid dynamical phenomena, and the resultant part quality is highly dependent on the process parameters (estimated to be around 50 in number) which affect the resultant surface quality and defects [19]. Liu et al. [20] experimentally compared the coolant flow rate and cooling performance of L-PBF printed cooling channels with that of drilled cooling channels, and found that both the flow rate and the cooling performance of the L-PBF printed cooling channels were inferior to that of drilled cooling channels due to low dimensional accuracy, the presence of unmelted particles, and the high surface roughness of the L-PBF printed cooling channels.

The shape deviation of an L-PBF printed internal channel depends on its printing orientation, with horizontally printed channels suffering the most severe deformation and vertically printed ones the least [21]. For a horizontally printed circular channel, the cross-sectional shape deforms to an ellipse due to thermal stress-induced warp [21]. The critical overhang angle (with respect to the build direction) is often recognized as 45° [22] beyond which support structures are usually required. A teardrop-shaped self-supporting structure, in which the upper half of a circular channel is replaced by a triangular roof with 45° inclines, was proposed to eliminate the overlarge overhang angle [2,23]. However, residual stresses concentrate at the top (i.e. the sharp corner) of the teardrop shape reducing mechanical (e.g. fatigue) strength, especially for thin-walled channels.

High surface roughness affects not only mechanical properties (such as a drop of fracture toughness) [24] but also fluid performance (pressure drop) [25,26] during injection molding. The surface roughness R$_a$ of an internal surface after L-PBF is usually around $10-20$ μm [2], much

greater than a traditionally-machined surface [23]. It has been reported that the channel orientation has a significant effect on the surface roughness of L-PBF printed interior channels [2,7]. Vertically printed interior channels have the smoothest interior surface [23]. Besides, the surface roughness is influenced by the slicing-induced staircase effect as the channel orientation angle increases from 0° (vertical) to 60° [2].

Under improper process conditions, other defects, such as pores, incomplete melting, and balling, are also found in L-PBF printed parts affecting their mechanical properties [3,5]. Porosity is formed under the keyhole regime caused by the boiling of the melt pool when employing an unsuitably large volumetric energy density [1]. Gong et al. [4] proposed that porosity less than 1 vol.% only has a slight effect on mechanical properties, while porosity greater than 5 vol.% considerably lessens tensile strength. On the contrary, porosity also results due to unmelted powder when the volumetric energy density is lower than the optimal value. Under this situation, even 1 vol.% porosity highly influences tensile strength and fracture toughness. According to the experimental results of Wei et al. [27], the porosity is significantly determined by volumetric energy density and hatch spacing, and the mechanical properties (tensile strength and fracture toughness) can be enhanced by decreasing porosity.

Scanning strategies are further divided into intra-layer strategy and inter-layer strategy. Orthogonal scanning and one way scanning are the most widely used intra-layer and inter-layer scanning strategies, respectively [28–30]. Zhang et al. [3] proposed that the horizontal accuracy is not affected by the angles of scanning tracks between layers due to cyclic processing. Yadroitsev and Smurov [31] proposed that the maximum hatch space should not exceed the average width of the continuous track to process a smooth surface.

Some studies were focused on prediction and compensation of the deformation. Zhang et al. [3] predicted the horizontal dimensional accuracy of vertically printed thin walls. The Newtonian fluid model was assumed to be applicable for the molten materials in the melt pool. It was concluded that the horizontal dimensional deviation is mainly caused by heat accumulation-induced track width and temperature history-dominated solidification shrinkage. Using their model to pre-compensate, the printing of Ti6Al4V thin-wall samples was achieved with a dimensional deviation of fewer than 20 μm. Kamat and Pei [21] proposed an analytical model to predict and compensate for the stress-induced deformation in overhanging regions of horizontally printed internal channels. The overhanging region was treated as a cantilever beam where the Euler-Bernoulli beam bending theory is applicable. The model was used to predict and compensate for the shape deviation (deformation) for three different shapes of channel cross-sections, i.e. circular (diameter of $8-12$ mm), elliptical (major axis of 12 mm, minor axis of $8-10$ mm), and diamond-shaped (vertical diagonal of 12 mm, angle of $80-100°$), and showed good agreement with the experimental results.

The present study focuses on the roundness and overhanging shape

deviation of horizontally printed small-diameter ($1-3$ mm) interior circular channels by considering the physics of melt pool behavior and thermal stress/strain development. The effect of one design parameter (designed inner diameter) and three process parameters (laser power, scanning speed and scanning strategy) on roundness and overhanging shape deviation is experimentally investigated using response surface methodology (RSM). Experiment-based regression models are developed according to the experimental results. Analysis of variance (ANOVA) shows the quality of the fit. Further, melt pool flow and volumetric strain in overhanging regions are simulated by developing a preliminary computational fluid dynamics (CFD) model to reveal the effect of thermo-mechanical behavior in the melt pool on the resultant diametric shape deviations and overhanging shape deviations. Finally, dual-objective optimization advice is proposed to minimize the roundness error and hang-diameter ratio.

2. Experimental methodology

2.1. Experimental setup and materials

An L-PBF machine (EP-M100 T, manufactured by SHINING 3D Tech. Co., Ltd., China) was employed in the present study. A random-polarized Gaussian beam was produced by a Yb: Glass fiber laser with a wavelength of 1080 nm. The focused beam diameter was 50 μm. The maximum laser power and laser scanning speed were 200 W and 8000 mm/s, respectively. The maximum build volume of the L-PBF machine was 120 mm × 120 mm × 80 mm. The processing was conducted in a protective nitrogen (N_2) atmosphere with a gas pressure of 2–3.5 kPa. The gas flow direction was from right to left (in the front view of the build chamber) which was perpendicular to the powder recoating direction. Materialise Magics and EPlus Hatch Tools were used as the pre-processing software that the former was for slicing and the latter was for parameter setting. Spherical powder of 316 L stainless steel was used as the experimental material in the present study. The powder size distribution and chemical composition are listed in Tables 1 and 2 respectively.

2.2. Experimental design by response surface methodology

In the present study, the interior channels with circular cross-section were printed horizontally without any support, i.e., the axial direction of the interior channels was perpendicular to the (vertical) build direction, as shown in Fig. 1. The channels were printed in cubic samples with a uniform size of 5 mm × 5 mm × 5.2 mm. The samples were placed on the build plate with the orientation of the channels parallel to the powder recoating direction. The designed inner diameter (also known as the nominal inner diameter, D_d, with a range of $1-3$ mm) of the interior channel and three process parameters related to the laser were chosen as the investigated factors. One of these three laser parameters, laser scanning strategy, is qualitative and the other two, laser power and scanning speed, are quantitative.

There is a correlation between laser power, scanning speed, and volumetric energy density [32]:

$$\Phi = \frac{P}{vht} \tag{1}$$

where Φ, P, v, h, and t are volumetric energy density, laser power, scanning speed, hatch distance, and layer thickness, respectively. The volumetric energy density is a measure of averaged applied energy per

volume of material, and was recommended to range from 40 to 200 J/mm^3 by the machine manufacturer. The range of laser power and scanning speed in the present study was thus determined following this recommendation and a pilot experimental result.

The manufacturer-recommended layer thickness was $20-100$ μm. The layer thickness was set as 80 μm to reduce print times and to ensure that the layer thickness was larger than the maximum powder size D_{90} (46.581 μm). The boundaries of each layer were double contoured following the printing of the volume region, applying the same process parameters as that of the volume region. The other process parameters were fixed as follows according to the recommendation of the manufacturer: a hatch distance of 60 μm for the volume region, a spacing of 80 μm between the outer boundary contour and the inner boundary contour, and a beam offset of 40 μm for the outer boundary contour.

The experimental design was conducted using Design-Expert software. RSM with Central Composite Design (CCD-RSM) was employed to design the experiments where 4 factors and 5 levels for each factor are applied, as listed in Table 3. The levels were coded as middle level (Level 0), low level (Level -1), high level (Level +1) and ± alpha levels (Level $\pm\alpha$) relevant to 3 types of points, i.e. center points, axial points, and factorial points, where the value of α was set as 1.6818. The center point was a point with all levels set to Level 0, the midpoint of each factor range, and was repeated 5 times to get a good estimate of experimental error. As a result, an experimental design with 95 runs was obtained.

Five laser scanning strategies, i.e. linear scanning with 0°, 45° and 90° intra-layer rotation, and grid-scanning (further divided into the small-grid scanning and the large-grid scanning), were performed in the experiments, as shown in Fig. 2. The fiducial scanning direction (0° direction) was from left to right, which was against the gas flow direction.

3. Regression model and its ANOVA

The L-PBF printed samples with different designed inner diameters are illustrated in Fig. 3. Though the designed cross-section of the interior channels was circular, the actual cross-section was no longer an ideal circle due to the effect of thermal stress and strain, as well as the shape and size of the melt pool, inducing anisotropic deformation. Besides, an inverted triangular hanging structure (dross) formed at the top of the interior channel in some cases, as shown in Fig. 4a. In the present study, the term hanging length is defined as the distance from the top of the designed channel circle to the tip (the lowest point) of the hanging structure, as schematically shown in Fig. 4b. Three indicators, namely actual horizontal diameter, actual vertical diameter, and hanging length were measured using an optical microscope. Due to the presence of the hanging structure hindering the measurement, the actual vertical diameter was estimated as twice the measured vertical radius of the lower half of the channel.

According to the measured indicators, two deduced responses representing the roundness and overhanging shape deviation for a horizontally printed interior channel (i.e. roundness error, E_R, and hang-diameter ratio, E_H, respectively) are defined as:

$$E_R = \frac{D_l - D_h}{D_d} \tag{2}$$

$$E_H = \frac{L_h}{D_d} \tag{3}$$

where, D_d, D_h, D_l, and L_h are designed inner diameter, actual horizontal diameter, actual vertical diameter, and hanging length, respectively.

To develop the regression models for E_R and E_H, ANOVA was automatically conducted using the Design-Expert software to evaluate the fitness of some potential model forms (e.g. linear, quadratic, and higher-orders). The linear model, which didn't include quadratic or higher-order terms (representing the interaction between process parameters), showed the best fit for the experimental results. Therefore, the

Table 1
Powder size distribution.

Powder size	D_{10}	D_{50}	D_{90}
Value (μm)	23.871	33.409	46.581

Table 2

Chemical composition of 316 L stainless steel powder.

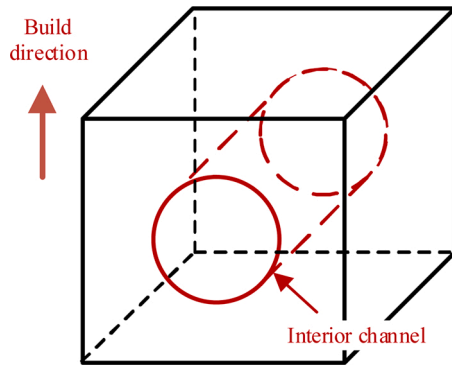| Element	C	Si	Mn	S	P	Cr	Ni	Mo	Fe
wt%	≤ 0.03	≤ 1.0	≤ 2.0	≤ 0.01	≤ 0.025	16.0 - 18.0	10.0 - 14.0	2.0 - 3.0	Bal.

Fig. 1. Schematic of the build direction of the interior channel.

Table 3

Parameters and their levels used in RSM design.

Factor	Level				
	-α	−1	0	1	α
A: Designed inner diameter (mm)	1.00	1.41	2.00	2.59	3.00
B: Laser power (W)	60.00	68.11	80.00	91.89	100.00
C: Scanning speed (mm/s)	150.00	190.54	250.00	309.46	350.00
D: Scanning strategy	Linear (0° rotation)	Linear (45° rotation)	Linear (90° rotation)	Grid (large)	Grid (small)

models were developed as:

$$E_R = F_1 - 0.019783A + 5.74041 \times 10^{-4}B - 2.07660 \times 10^{-4}C \quad (4)$$

$$E_H = F_2 - 0.063559A + 3.39107 \times 10^{-3}B - 6.03701 \times 10^{-4}C \quad (5)$$

where, A, B, and C are designed inner diameter (mm), laser power (W), and scanning speed (mm/s), respectively; F_1 and F_2 are coefficients related to scanning strategy and derived from the fitting, as listed in Table 4.

The ANOVA for these models showed their goodness of fit, as listed in Table 5. The model p-value for Model E_R that was 0.04 implied that the model was significant and there was only a chance of 4% that a model F-value as large as listed in Table 5 could occur due to noise. For Model E_H, the chance that a model F-value this large could occur due to noise was even less than 0.01 % as its p-value was less than 0.0001. The lack of fit F-values for E_R and E_H, 1.27 and 1.92, respectively, implied that the lack of fit was not significant relative to the pure error and there were chances of 28.37 % and 5.31 %, respectively, that a lack of fit F-values this large could occur due to noise. Consequently, the models were with good significance as the lack of fit was insignificant. In addition, the predicted R-squared was in reasonable agreement with the adjusted R-squared, whose difference was less than 0.2. The adequate precision, measuring the signal to noise ratio that a value greater than 4 is desirable, was 6.376 and 23.438 for E_R and E_H respectively, meaning an adequate signal for each model, and indicating the models could be used to navigate the design space.

Therefore, the effect of designed inner diameter, laser power, and scanning speed on roundness error and hang-diameter ratio, is illustrated by perturbation plots, as shown in Fig. 5. Each curve in the plots corresponded to the variation of a single parameter while the scanning strategy was set as linear with 0° rotation (Level –α) and the other two
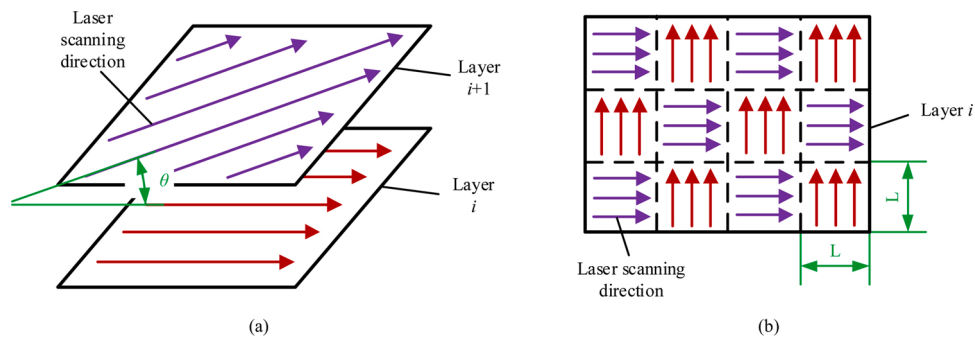

Fig. 2. Schematic of laser scanning strategies: (a) linear scanning ($\theta = 0°$, 45°, and 90°, respectively) and (b) grid-scanning ($L = 2.5$ mm for large-grid scanning and 0.5 mm for small-grid scanning).
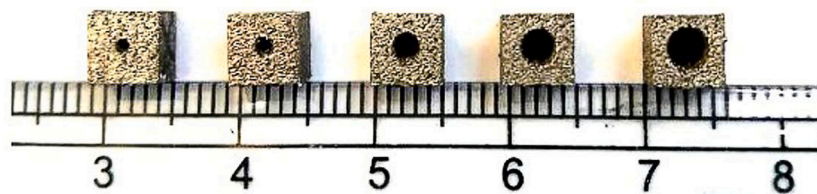

Fig. 3. L-PBF printed samples with different designed inner diameters (from left to right: $D_d = 1.00$, 1.41, 2.00, 2.59, and 3.00 mm, respectively).
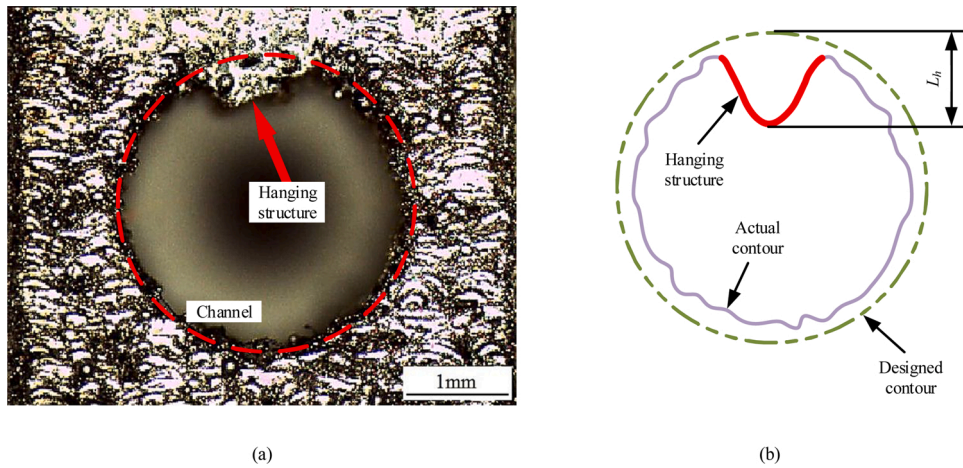
Fig. 4. A hanging structure (dross) formed at the top of an interior channel.

Table 4
Coefficients F_1 and F_2 under different scanning strategies.

Scanning strategy	F_1	F_2
Linear (0° rotation)	0.086072	0.26349
Linear (45° rotation)	0.090690	0.22527
Linear (90° rotation)	0.099963	0.24255
Grid (large)	0.099349	0.30241
Grid (small)	0.088911	0.34005

parameters were set to a constant of Level 0, as listed in Table 3. The uniform coded units of parameters were applied to replace their natural units. The conversion between uniform coded units and natural units were calculated by

$$V_C = \frac{\alpha(V_N - V_0)}{V_\alpha - V_0} \tag{6}$$

where, V_C and V_N are parameter values in terms of a uniform-coded unit and the natural unit, respectively; V_0 and V_α are the values in terms of the natural unit for the parameters at Level 0 and Level $+\alpha$, respectively.

4. Development of a simulation model

A 3D simulation model was developed using the commercial CFD software Flow-3D to explain the experimental results preliminarily. A single-track scanning process was simulated so that the laser scans from the solid region to the overhanging region. The dimensions of the geometry model are illustrated in Fig. 6. The powder was in uniform size

Table 5
ANOVA for regression models (Eqs. 4 and 5).

| Source	Sum of squares	DOF	Mean square	F value	p-value Prob > F	Significance
E_R: Roundness error						
Model	0.0261	7	3.723×10^{-3}	2.22	0.04	Significant
Residual	0.1459	87	1.677×10^{-3}			
Lack of fit	0.1181	67	1.762×10^{-3}	1.27	0.2837	Not significant
Pure error	0.0278	20	1.391×10^{-3}			
E_H: Hang-diameter ratio						
Model	0.4404	7	6.292×10^{-2}	25.3	< 0.0001	Significant
Residual	0.2114	85	2.487×10^{-3}			
Lack of fit	0.1821	65	2.802×10^{-3}	1.92	0.0531	Not significant
Pure error	0.0293	20	1.463×10^{-3}			
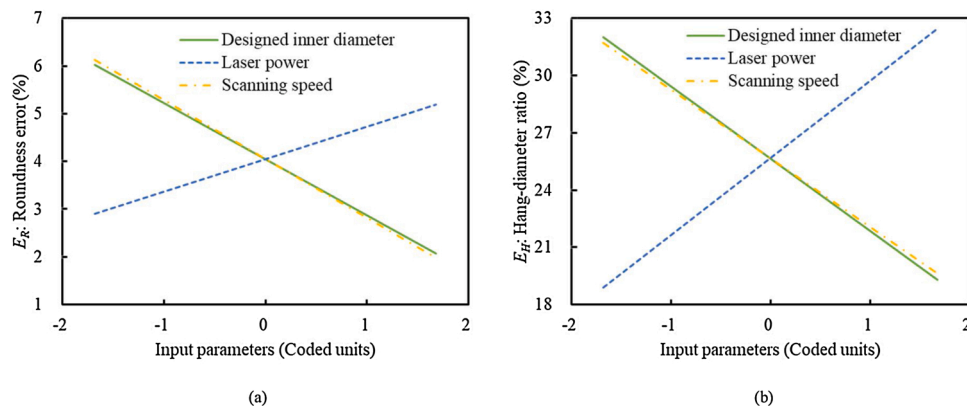
Fig. 5. Perturbation plots for the effect of designed inner diameter, laser power, and scanning speed on (a) roundness error and (b) hang-diameter ratio.

with a diameter of 22 μm. The powder packing was generated using SolidWorks and then imported into the model via an STL file. All the boundaries were treated as continuous. The effects of gravity, viscosity, surface tension, heat transfer, and solidification were considered in the simulation. The modeling space was meshed by cubic cells with a size of 5 μm. The workstation was configured with an Intel Core i5-3470 CPU (4 cores with 3.20 GHz frequency) and 8 GB DDR3 memory. The material properties used in the simulations are listed in Table 6. The simulation results on melt flow and volumetric strain will be illustrated in Sections 5 & 6.

5. Discussion on the formation mechanisms of diametric deviation

The shape deviation related to the diameter, typically represented by the roundness error (defined in Eq. 2), can be further divided into two sub-errors in orthogonal directions, i.e. horizontal diametric error and vertical diametric error. The sources and formation mechanisms of these two sub-errors are similar but their dominant factors are different. Two factors, namely the shape and size of the melt pool and thermal stresses, mainly determine the diametric deviation of an interior circular channel. These two factors influence oppositely the vertical diametric error, and which one plays the dominant role depends on the channel diameter and process parameters. Meanwhile, the horizontal diametric error is more affected by the shape and size of the melt pool rather than thermal stresses. In addition, the beam offset and slicing algorithm also affect the shape deviation to some extent.

5.1. Deviation determined by melt pool

During L-PBF, a melt pool is formed in the laser-material interacting zone. The melt (and solidification) front moves along with the scanning laser beam. The formation of the solid is actually on account of the so-lidification of the melt pool. The size and shape of the melt pool thus heavily influence the final contour as well as the shape deviation.

5.1.1. Effect of the melt pool on horizontal diametric deviation

Imagining the trajectory of the laser spot center is aligned with the designed boundary when the laser beam scans the boundary of a solid area, the printed boundary thus doesn't coincide with the designed boundary. The deviation between designed and actually printed boundaries depends upon the width of the melt pool. Theoretically, this is equal to the half-width of the melt pool, as shown in Fig. 7a. A beam offset is usually employed in L-PBF to compensate for the deviation induced by the melt pool. There are three situations of beam offset with respect to the deviation induced by the melt pool: i) the beam offset is smaller than the half-width of the melt pool (Fig. 7b), ii) the beam offset is equal to the half-width of the melt pool (Fig. 7c), or iii) the beam offset is larger than the half-width of the melt pool (Fig. 7d). The situation shown in Fig. 7c is the ideal situation where the beam offset can exactly compensate for the deviation induced by the melt pool. Since the size of the melt pool depends on the volumetric energy density (which will be

Table 6
Material properties used in the simulations.

Properties	Value
Density (kg/m^3)	Solid: 7260, liquid: 7249
Specific heat (J/kg K)	Solid: 722, liquid: 726
Thermal conductivity (W/m K)	Solid: 29.35, liquid: 28.95
Liquidus temperature (K)	1697.15
Solidus temperature (K)	1674.15
Volumetric thermal expansion (1/K)	1.73×10^{-5}
Latent heat of fusion (J/kg)	2.6×10^5
Surface tension (N/m)	$1.8225 - 4.226 \times 10^{-4}(T - 1774)$
Bulk modulus (GPa)	163
Shear modulus (GPa)	77.2
Elastic modulus (GPa)	200
Poisson ratio	0.305
Yield stress (MPa)	205

further discussed in Section 5.3.2), the ideal beam offset varies with process parameters. Since a constant beam offset (40 μm) is used, the situation shown in Fig. 7b applies to the present study, namely, the beam offset is smaller than the half-width of the melt pool (the former cannot compensate for the deviation induced by the melt pool completely). The following discussions are thus in light of this situation.

As shown in Fig. 7b, the actual channel built on each layer is narrower than the designed one. When horizontally building an interior channel layer by layer, there is a horizontal offset between designed and actually printed contours, as shown in Fig. 8. Therefore, the actual inner diameter in the horizontal direction is smaller than the designed one. This horizontal diametric error is mainly induced by the width of the melt pool. The offset between the designed and actually printed boundaries increases with the increased width of the melt pool.

It must be noted that thermal conduction between powder particles is essentially a heat transfer process from powder to gas to powder. The effective thermal conductivity of a powder bed is strongly determined by the thermal conductivity of the gas due to gaps between powder particles. Hence, the thermal conductivity of a powder bed is much smaller than that of a solid. Ref. [33], in which experiments were conducted at temperatures from 295 to 470 K, found that the thermal conductivity of a powder bed ($\sim$0.05 W m^{-1} K^{-1}) is two orders of magnitude smaller than that of a solid (13.4 W m^{-1} K^{-1}). Moreover, the thermal conductivity of a powder bed remains essentially constant at a gas pressure of 1.6 kPa, which is close to the gas pressure range used in the present study. At a lower thermal conductivity, thermal energy in the melt pool cannot be conducted to the surrounding fast enough, resulting in heat accumulation and thus an increase in the melt dimensions. Therefore, as shown in the simulation results in Fig. 9, the width of the melt pool at the overhanging regions is more than in the 'core' regions due to the lower thermal conductivity of powder, which further contributes to the horizontal diametric error for internal channels. Moreover, similar findings were also proposed by Safdar et al. [34] and Kamara et al. [35] despite that they studied different thermal conductivity for the liquid phase but not the solid phase.
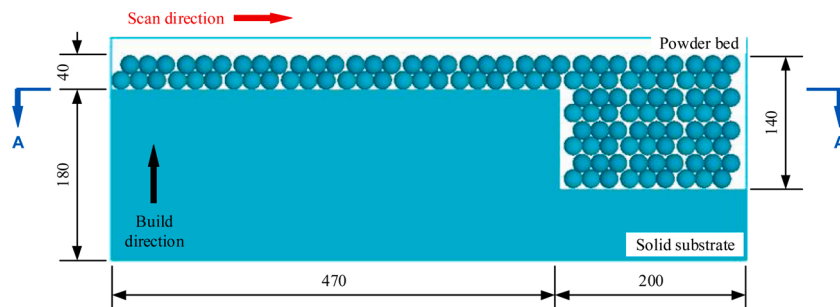

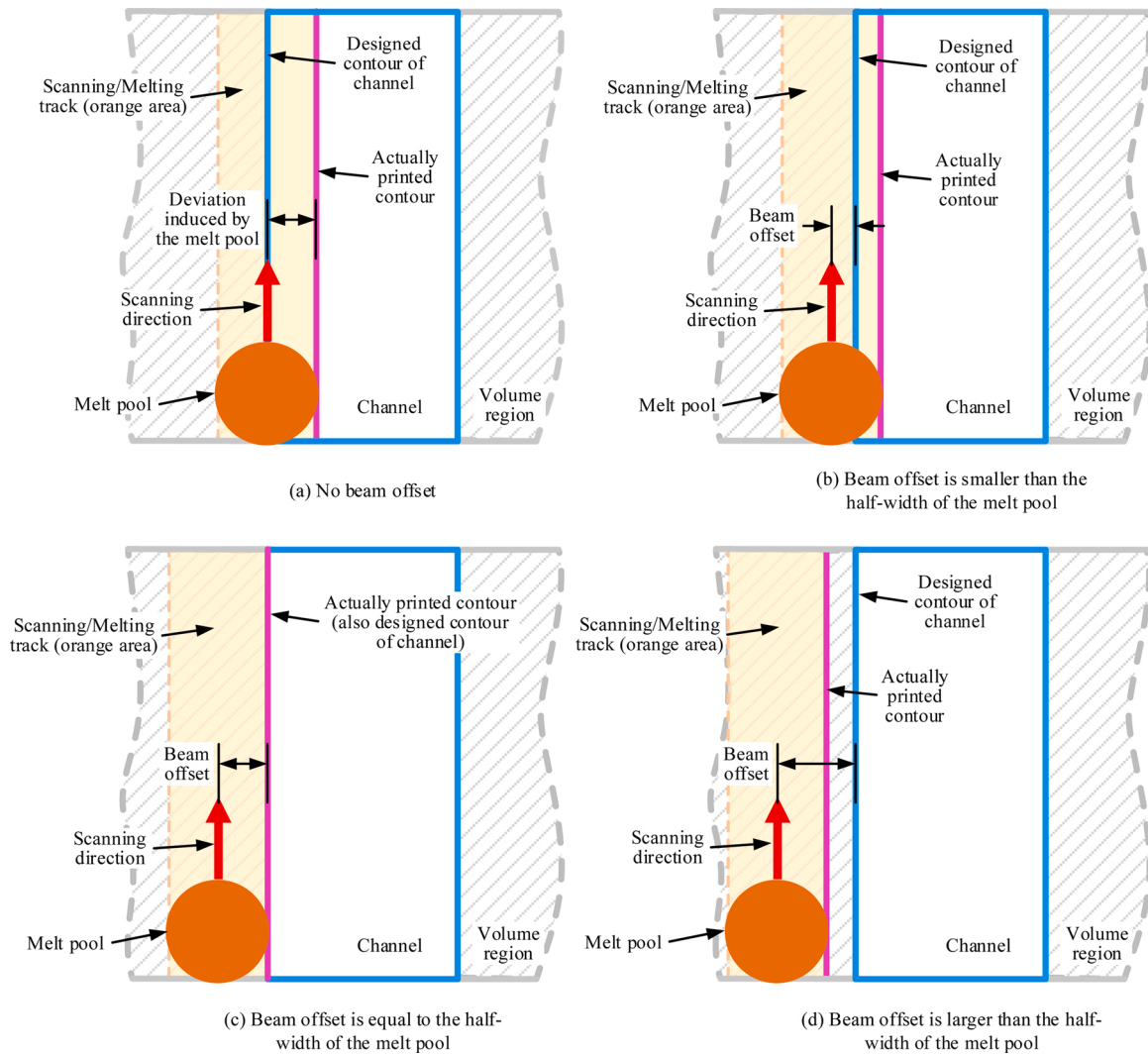**Fig. 6.** The dimensions of the geometry model (unit: μm).

Fig. 7. Beam offset with respect to the deviation induced by the melt pool.

(a) No beam offset

(b) Beam offset is smaller than the half-width of the melt pool

(c) Beam offset is equal to the half-width of the melt pool

(d) Beam offset is larger than the half-width of the melt pool

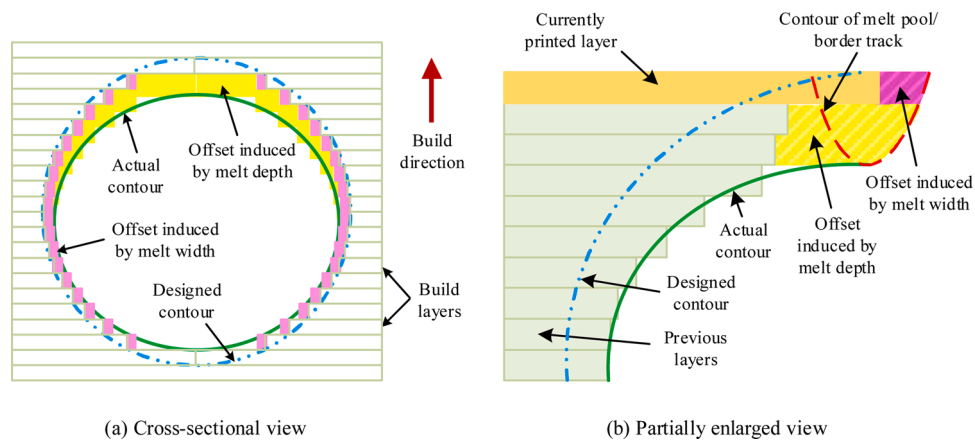(a) Cross-sectional view

(b) Partially enlarged view

Fig. 8. Offset between designed and printed contours induced by the melt pool.

5.1.2. Effect of the melt pool on vertical diametric deviation

As discussed in Section 5.1.1, the width of the melt pool affects the horizontal diametric deviation of a horizontally printed interior channel. Similarly, its vertical diametric error is influenced by the depth of the melt pool. It is shown in Fig. 8b that the depth of the melt pool is larger than the layer thickness. The melt depth-to-layer thickness ratio is usually more than 2 [36]. This ensures that not only the currently printed layer but also the previously printed layer(s) is/are melted and re-solidified under the laser heating effect which is necessary for efficient bonding. For solid regions (i.e. with no overhangs), this behavior leads to thermal residual stresses accompanied by slight deformation. For overhanging regions, however, the layers below the currently
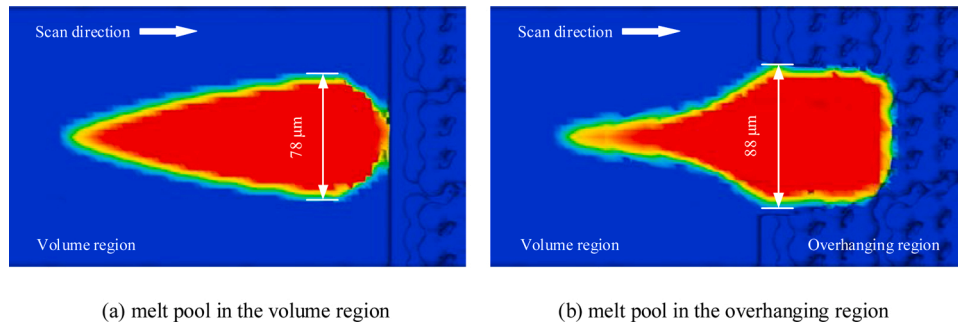
(a) melt pool in the volume region   (b) melt pool in the overhanging region

Fig. 9. Shapes of the melt pool in the volume region and overhanging region (on the A-A cross-section marked in Fig. 6).

printed layer are unmelted and hence in powder form. Due to the large depth of the melt pool, the powder bed below the currently printed layer which ideally should not be processed is nevertheless melted and fused to the bottom of the overhanging region. As a result, the final vertical diameter of a horizontally printed interior channel is smaller than the designed diameter.

In L-PBF, in addition, a solid model is sliced into layers, and the sliced contour is step-like. Due to the slicing algorithm, the step end is inside the designed contour, as shown in Fig. 8a. This also results in the printed contour being smaller than the designed one in both horizontal and vertical directions.

5.2. Deformation induced by thermal stresses

Besides being affected by the shape and size of the melt pool, the vertical diametric error is highly affected by thermal stresses and the induced plastic strains. During laser-materials interaction, there are complex melt pool dynamics, e.g. heat transfer, phase transition, and turbulent flow driven by Marangoni convection [37]. The different heating and cooling rates induce temperature differences in the melt pool, causing thermal stresses in the solidified solid layers. Residual stresses are partly relieved by the material undergoing deformation especially in thinner sections. Hence there is a tendency for the layers to warp up. In general, the larger and thinner the layer, the more pronounced the deflection. This especially affects overhanging regions that are built without support. It has been shown in the literature [38] that overhanging regions exhibit more deviation but lower residual stresses, in contrast to the volume region where the residual stresses are higher but the deviation is much lower.

The L-PBF of a horizontal internal channel essentially entails printing a cantilever of variable cross section, as shown in Fig. 10. The left part (green region) is constrained by layer(s) below, indicating a strong stiffness, and thus suffers little deflection. On the other hand, the cantilever part on the right (yellow region) is unconstrained and will be more deflected due to stress relief. At the upper half of the channel, the overhang angle increases with the number of printed layers, resulting in the increase of the cantilever length and thus more significant deflection.

The deflection in the overhanging (cantilever) region discussed above and schematically shown in Fig. 10 is justified by the simulation-predicted volumetric strain illustrated in Fig. 11. In this figure, negative volumetric strain indicates a shrinkage while positive volumetric strain indicates an expansion. Two main things can be concluded: firstly, the volumetric strain in the overhanging region is evidently at a much higher level than in the solid region, especially for the shrinkage strain, indicating that the constraints in the solid region restrain the deformation; and secondly, in the overhanging region, the upper half shrinks (circled in red) while the lower half expands (circled in black). As a result, the upper half pulls the lower half upwards, causing the deflection of the overhanging region. Therefore, the cantilever part warps up and the channel is elongated in the vertical direction.
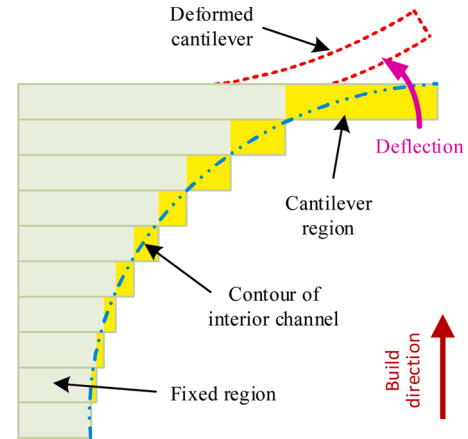

Fig. 10. Schematic of the deflection in the overhanging region.

As discussed above, the displacement (deflection) is mainly manifested in the vertical direction while the displacement in the horizontal direction is negligible. Thus, the horizontal diametric error is hardly affected by thermal stresses.

5.3. Effect of process parameters on roundness error

From the experimental results, it is seen that the as-printed diameter is smaller than the designed diameter. The diametric deviation varies with direction. As discussed in Sections 5.1 & 5.2, the roundness error is a combined consequence of horizontal diametric error and vertical diametric error, which are affected by shape and size of the melt pool, thermal stresses, beam offset, and slicing algorithms. The effect of these factors on actually printed horizontal and vertical diameters is summarized in Table 7.

It is seen that the shape/size of the melt pool and slicing algorithms lessen the actually printed diameter in both horizontal and vertical directions. Thermal stresses enlarge the actually printed vertical diameter but have little effect on horizontal diametric error. In contrast, beam offset enlarges the actually printed horizontal diameter but influences vertical diametric error hardly. This indicates the shape deviation caused by the shape/size of the melt pool and slicing algorithms can be compensated by the thermal stresses-induced deformation (in the vertical direction) and beam offset (in the horizontal direction) to some extent.

5.3.1. Effect of designed inner diameter on roundness error

Strictly, the designed inner diameter is a design parameter but not a process parameter. The factor(s) dominating the diametric error is/are related to the designed inner diameter. Because the actual vertical and horizontal diameters are slightly smaller than the designed ones, for interior channels with small inner diameters (1−3 mm), the shape/size
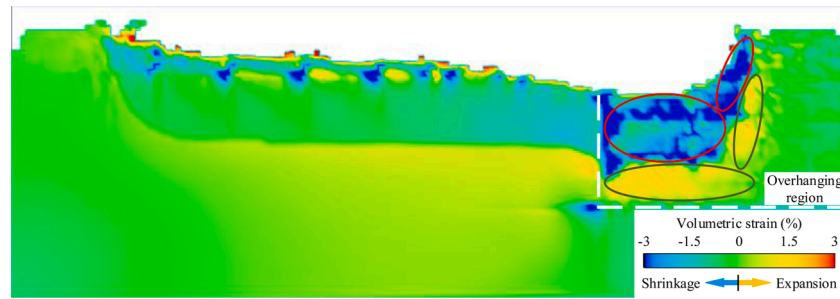
Fig. 11. Volumetric strain in the overhanging region.

Table 7

Effect of four factors on actually printed horizontal and vertical diameters.

Influencing factors	Actually printed horizontal diameter	Actually printed vertical diameter
Shape and size of the melt pool	Lessening	Lessening
Thermal stresses	Neglected	Enlarging
Beam offset	Enlarging	Neglected
Slicing algorithms	Lessening	Lessening

of the melt pool and the slicing algorithm dominate the vertical and horizontal diametric errors.

The shape and size of the melt pool are independent of the designed inner diameter. When increasing the designed inner diameter, the ratios of layer thickness to the designed inner diameter and depth of the melt pool to designed inner diameter decrease correspondingly. The relative vertical diametric error decreases in spite of the absolute vertical diametric error keeping constant. Similarly, the relative horizontal diametric error decreases due to the constant absolute horizontal diametric error and the decreased ratio of the width of the melt pool to the designed inner diameter. As a result, the roundness error is negatively proportional to the designed inner diameter according to Eq. 2, as shown in Fig. 5a.

5.3.2. Effect of laser power and scanning speed on roundness error

The shape and size of the melt pool, namely melting width and depth, mainly depend on laser spot size and volumetric energy density, the latter of which is calculated by Eq. 1. When the laser spot size is kept as a constant, the size of the melt pool is only determined by the volumetric energy density. In other words, an increased volumetric energy density leads to an increased melting width and melting depth, leading to an increase in the horizontal and vertical diametric errors consequently. Moreover, the increased volumetric energy density leads to the increase of temperature difference and thus thermal stresses, inducing more significant warpage and compensating partially for the diametric error induced by the shape/size of the melt pool in the vertical direction. Therefore, the increment of the vertical diametric error is less than the increment of the horizontal diametric error, resulting in an increase in the roundness error according to Eq. 2.

According to Eq. 1, either an increase of laser power or a decrease of scanning speed results in an increase of volumetric energy density, indicating that the increased laser power raises the roundness error while the increased scanning speed reduces it.

5.3.3. Effect of scanning strategy on roundness error

In Eqs. 4 & 5, there is a constant term, F, whose value listed in Table 4 is dependent on scanning strategy indicating the effect of scanning strategy on roundness error and hang-diameter ratio. It can be concluded from the equations that in spite of the scanning strategy influencing roundness error and hang-diameter, it doesn't affect their changing trend and changing rate with the other process parameters (i.e.

designed inner diameter, laser power, and scanning speed). In other words, for two specified scanning strategies, the difference in either roundness error or hang-diameter ratio is the same under varying designed inner diameter, laser power, or scanning speed.

It is seen in Table 4 that the 0° rotational linear scanning approach and small grid scanning approach result in the smallest and second smallest roundness errors, respectively. Meanwhile, the 90° rotational linear scanning and large grid scanning approaches result in the worst roundness. The effect of scanning strategy on roundness error is not significant indicating that the difference in roundness error between the best and the worst situations is about 1.4 %.

It should be noted that there is usually a considerable effect of gas flow direction with respect to the scanning direction on printing quality. It is found in the literature that it mainly affects the ultimate tensile strength, compression strength, and porosity as the spattered powder may be blown into the laser scanning path resulting in contamination [39–41]. Although there is no convincing evidence in the literature up to now, the gas flow direction may introduce anisotropy in residual stresses. In the present study, all channels were printed in the same orientation with respect to the gas flow direction so as to assume they were affected by the gas flow direction all equally. Further investigations may be conducted focusing on the effect of gas flow direction in the future.

6. Discussions on the formation mechanisms of hanging structure

As introduced in Section 3, there is an inverted triangular hanging structure (i.e. dross formation) at the top of the interior channel. This dross is a considerably significant defect for L-PBF printed interior channels with small inner diameters ranging from 1 to 3 mm. It is seen in Fig. 5b that the hang-diameter ratio can even be as high as 32 % in a 1 mm diameter interior channel. According to the experimental results obtained by us and in the literature [21], the dross is not significant for L-PBF printed interior channels with larger diameters ($\geq$ 8 mm). This indicates that the hanging length, as well as the hang-diameter ratio, is highly dependent on the designed inner diameter. The cross-sectional profiles of the overhanging regions of interior channels with different designed inner diameter are illustrated in Fig. 12. The profiles are measured by a laser confocal microscope (Keyence VK-X200).

Besides the inner diameter, volumetric energy density is another important factor influencing the formation of a hanging structure. Fig. 13 illustrates the simulation result on the propagation of a melt pool from a solid region to an overhanging region. In an overhanging region as shown in Fig. 13c, the melt pool is supported by unconsolidated powder rather than a solid structure. There are gaps between the powder. Due to gravity, the molten material flows downward into the gaps, partially sintering the powder particles and sinking the melt pool (Fig. 13d). During this process, some powder below the designed overhanging region is surrounded and melted by the molten materials, becoming a part of the melt pool. Dross formation thus occurs in the overhanging region after solidification of the melt pool, as shown in
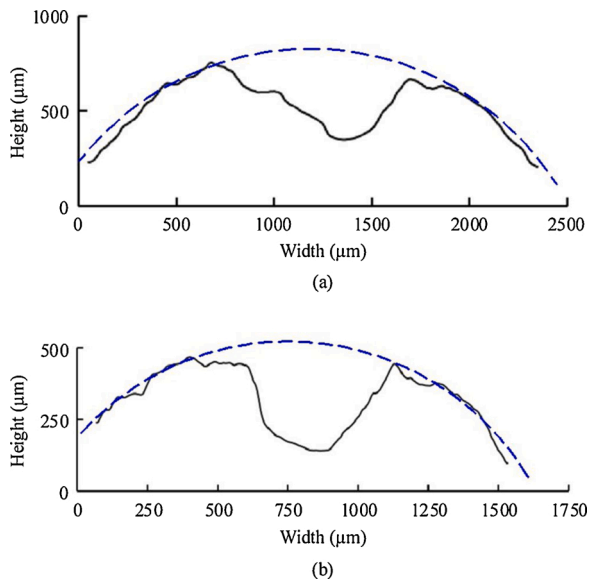
Fig. 12. Cross-sectional profiles of overhanging region: (a) $D_d = 3$ mm and (b) $D_d = 2$ mm ($P = 80$ W, $v = 250$ mm/s, large grid scanning approach; black solid lines: actual profiles; blue dotted lines: theoretical profiles) (For interpretation of the references to colour in this figure legend, the reader is referred to the web version of this article).

Fig. 13e. In addition, as discussed in Section 5.1.1, thermal energy in the melt pool cannot be conducted to the surrounding fast enough when printing an overhanging region due to the numerous gaps and thus the low thermal conductivity, resulting in the deepening of the melt pool. Also, the viscosity of the molten materials decreases (indicating a better fluidity) with increasing melt pool temperature. These behaviors further contribute to the formation of the hanging structure. With the increase of volumetric energy density, the melt pool becomes larger and the viscosity becomes smaller, exacerbating the sinking of the melt pool. When the volumetric energy density exceeds the threshold, the melt pool above the powder bed would collapse due to overlarge surface tensions, interrupting the printing.

At the edges of the melt pool, some powder may be partially melted. Meanwhile, some unmelted powder may adhere to the edges of the melt pool. It enlarges the hanging structure and roughens the profile. This phenomenon becomes more prominent with the increasing volumetric energy density. It is seen in Fig. 12 that the profile of the hanging structure is irregular, indicating the complex thermo-mechanical behavior in the melt pool and the randomness of the formation process of dross.

The increasing overhang angle decreases the contact area of the melt pool with the solid region, leading to a poorer thermal conductivity and a larger hanging structure. The overhang angle varies in a circular interior channel, increasing closer to the zenith of the channel. Consequently, the cross-sectional profile of a hanging structure is approximately inverted triangular. There are two approaches to address this problem. The first one is to add supports for overhanging regions improving the thermal conduction, which is not applicable to the cases in this study. The second one is to set different process parameters for overhanging regions from that for solid regions; for example, smaller laser power and/or higher scanning speed, reducing the volumetric energy density on overhanging regions [42].

The experimental result shows that the hanging length slightly increases with the increasing designed inner diameter. This indicates the sinking of the melt pool is boosted when printing a larger diameter channel. However, the increment of hanging length is much smaller than the increment of designed inner diameter.

The effect of scanning strategy on the hang-diameter ratio was

discussed in Section 5.3.3. It is seen in Table 4 that the 45° rotational linear scanning approach results in the smallest hang-diameter ratio, while the small grid scanning approach results in the largest hang-diameter ratio. The effect of scanning strategy on the hang-diameter ratio is much more significant than that on roundness error. The difference in the hang-diameter ratio between the best and the worst situations is as high as 11.5 %.

7. Dual-objective optimization advice

There are two ways to minimize the shape deviations in the horizontally printed interior channels. The one is to compensate for the deviation in the design stage, namely the L-PBF-oriented design [21]. The other one is to reduce the melt pool size at the boundaries and improve the thermal cycle by optimizing the process parameters. The former is an effective way to reduce the roundness error. However, it is unsuitable for the minimization of hanging structures because the shape of a hanging structure is too irregular and random to be predicted and compensated by modifying the pre-print design.

The problem of minimizing the shape deviation on both the roundness error and the hang-diameter ratio is a dual-objective optimization problem. As the designed inner diameter is a design parameter but not a process parameter, it should be selected according to the design requirement but not be optimized. From the regression models developed in Section 3, the relationships between the results and the parameters are linear, and there is no interaction between parameters. According to the model monotonicity, therefore, small laser power or large scanning speed benefits reducing the roundness error and hang-diameter ratio. It is not possible to select a scanning strategy for optimizing both the roundness error and hang-diameter ratio, as the effect trends of scanning strategy on them are different. When the roundness error takes priority, the scanning strategy is optimized as 0° rotational linear scanning. When the hang-diameter ratio takes priority, the scanning strategy is optimized as 45° rotational linear scanning.

8. Conclusions

This paper studied the roundness and overhanging shape deviation of horizontally L-PBF-printed small-diameter (1−3 mm) interior circular channels, by conducting RSM experiments and developing a preliminary CFD simulation model. It is found that the roundness error is mainly affected by the shape and size of the melt pool and thermal stresses, while the beam offset and slicing algorithm also contribute to the roundness error to some extent. Formation of overhanging shape deviation, namely the hanging structures, is highly determined by the thermo-mechanical driven molten flow in the melt pool.

The printed cross-sectional profile of a circular interior channel is anisotropically deformed that the deformation in horizontal and vertical directions is different, inducing a roundness error. Although the absolute vertical and horizontal diametric errors remain constant with a decreasing designed inner diameter, the relative vertical and horizontal diametric errors increase resulting in the increase of roundness error. To decrease the roundness error, in addition to choosing a proper beam offset, the size (both width and depth) of the melt pool should be minimized by minimizing the volumetric energy density (smaller laser power or higher scanning speed).

Although thermal stresses should be minimized during the process, the vertical deformation is partially compensated due to the deflection accompanying the relief of thermal stresses on the weakly-constrained overhanging regions. The simulation results showed that the volumetric strain in the overhanging region is much more than in the solid region. Besides, there is a strong upwards pull effect causing deflection of the overhanging region due to the significantly differential shrinkage and expansion in the upper half and the lower half of the overhanging region respectively.

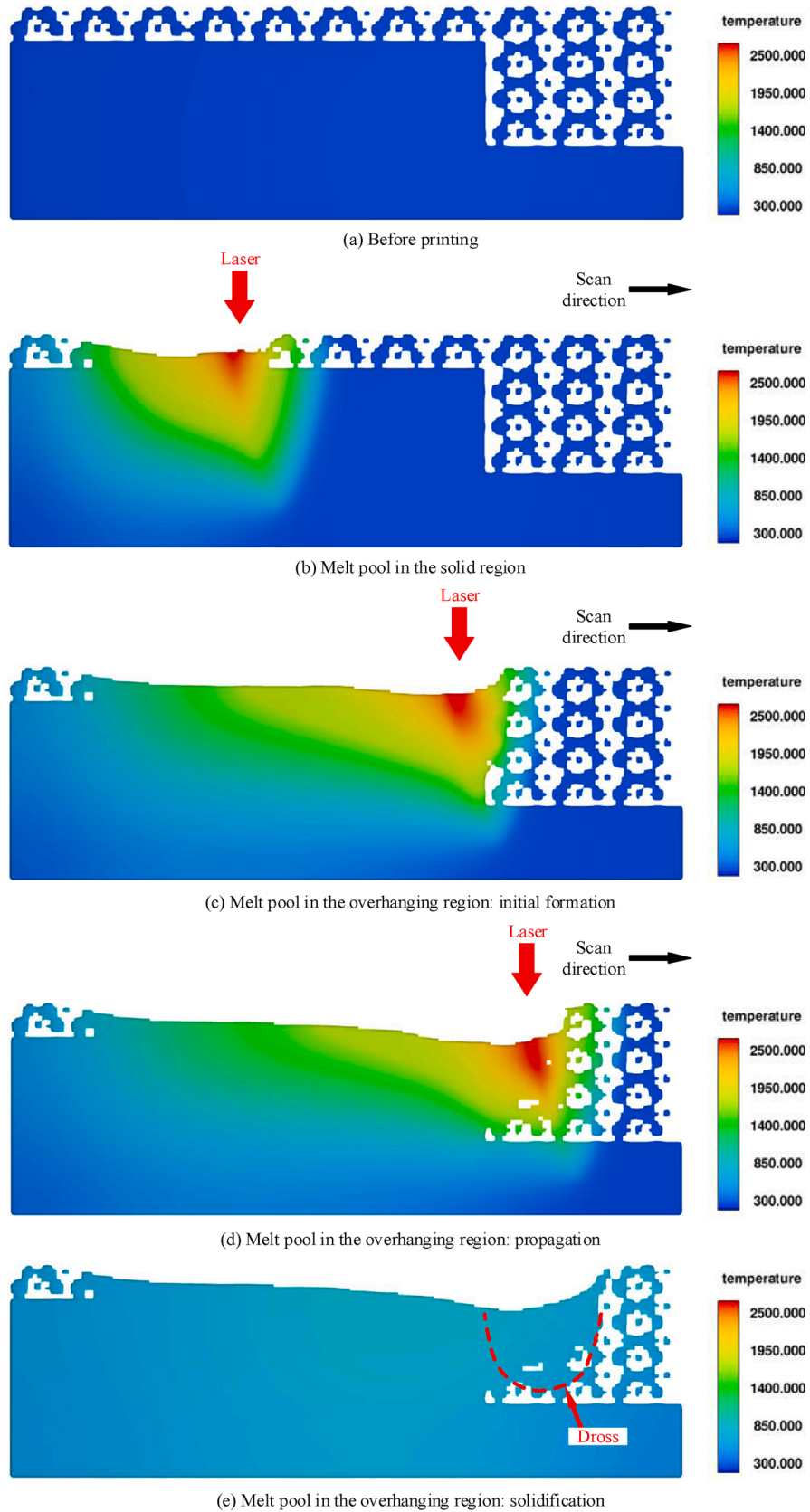0° rotational linear scanning approach and 90° rotational linear

(a) Before printing

(b) Melt pool in the solid region

(c) Melt pool in the overhanging region: initial formation

(d) Melt pool in the overhanging region: propagation

(e) Melt pool in the overhanging region: solidification

Fig. 13. Simulation result on the propagation of melt pool from the solid region to the overhanging region (scale unit: K).

scanning approach showed the smallest and largest roundness errors, respectively. However, the effect of scanning strategy on roundness error was not very significant and the difference in roundness error between the best and the worst situations was about 1.4 %.

Hanging structures with irregular profiles (dross) were formed due to the sinking of the melt pool on an unconsolidated powder bed under the effect of gravity, surface tension, and poor thermal conductivity. The more volumetric energy density on overhanging regions, the larger the hanging length. (Partially) unmelted powder randomly adhered to the edges of the melt pool enlarging the hanging structure and roughening the profile. A small-diameter interior channel is much more sensitive to dross than a large-diameter interior channel. The increment of hanging length was much smaller than the increment of the designed inner diameter. The effect of scanning strategy on the hang-diameter ratio was much more significant than that on roundness error. 45° rotational linear scanning approach derived the smallest hang-diameter ratio, while the small grid scanning approach resulted in the largest hang-diameter ratio. The difference in the hang-diameter ratio between the best and the worst situations was 11.5 %.

Finally, dual-objective optimization advice on minimizing the roundness error and hang-diameter ratio was proposed. Small laser power or large scanning speed benefited reducing the roundness error and hang-diameter ratio. 0° or 45° rotational linear scanning strategy was selected for obtaining the minimized roundness error or the minimized hang-diameter ratio, respectively.

CRediT authorship contribution statement

Shaochuan Feng: Conceptualization, Methodology, Formal analysis, Writing - original draft, Writing - review & editing, Visualization, Funding acquisition. **Shijie Chen:** Formal analysis, Investigation, Visualization. **Amar M. Kamat:** Writing - review & editing. **Ru Zhang:** Investigation. **Mingji Huang:** Project administration. **Liangcai Hu:** Resources.

Declaration of Competing Interest

The authors declare that they have no known competing financial interests or personal relationships that could have appeared to influence the work reported in this paper.

Acknowledgments

References

[1] I. Yadroitsev, P. Krakhmalev, I. Yadroitsava, Hierarchical design principles of selective laser melting for high quality metallic objects, Addit. Manuf. 7 (2015) 45–56, https://doi.org/10.1016/j.addma.2014.12.007.

[2] J. Pakkanen, F. Calignano, F. Trevisan, M. Lorusso, E.P. Ambrosio, D. Manfredi, P. Fino, Study of internal channel surface roughnesses manufactured by selective laser melting in aluminum and titanium alloys, Metall. Mater. Trans. A 47 (2016) 3837–3844, https://doi.org/10.1007/s11661-016-3478-7.

[3] L. Zhang, S. Zhang, H. Zhu, Z. Hu, G. Wang, X. Zeng, Horizontal dimensional accuracy prediction of selective laser melting, Mater. Des. 160 (2018) 9–20, https://doi.org/10.1016/j.matdes.2018.08.059.

[4] H. Gong, K. Rafi, H. Gu, G.D. Janaki Ram, T. Starr, B. Stucker, Influence of defects on mechanical properties of Ti–6Al–4V components produced by selective laser melting and electron beam melting, Mater. Des. 86 (2015) 545–554, https://doi.org/10.1016/j.matdes.2015.07.147.

[5] J. Günther, S. Leuders, P. Koppa, T. Tröster, S. Henkel, H. Biermann, T. Niendorf, On the effect of internal channels and surface roughness on the high-cycle fatigue performance of Ti-6Al-4V processed by SLM, Mater. Des. 143 (2018) 1–11, https://doi.org/10.1016/j.matdes.2018.01.042.

[6] I. Yadroitsev, L. Thivillon, P. Bertrand, I. Smurov, Strategy of manufacturing components with designed internal structure by selective laser melting of metallic

[7] J. Mingear, B. Zhang, D. Hartl, A. Elwany, Effect of process parameters and electropolishing on the surface roughness of interior channels in additively manufactured nickel-titanium shape memory alloy actuators, Addit. Manuf. 27 (2019) 565–575, https://doi.org/10.1016/j.addma.2019.03.027.

[8] E. Uhlmann, A. Bergmann, W. Gridin, Investigation on additive manufacturing of tungsten carbide-cobalt by selective laser melting, Procedia Cirp 35 (2015) 8–15, https://doi.org/10.1016/j.procir.2015.08.060.

[9] Y. Wang, K.M. Yu, C.C.L. Wang, Spiral and conformal cooling in plastic injection molding, CAD Comput. Aided Des. 63 (2015) 1–11, https://doi.org/10.1016/j.cad.2014.11.012.

[10] K.M. Au, K.M. Yu, A scaffolding architecture for conformal cooling design in rapid plastic injection moulding, Int. J. Adv. Manuf. Technol. 34 (2007) 496–515, https://doi.org/10.1007/s00170-006-0628-x.

[11] Y. Wang, K.-M. Yu, C.C.L. Wang, Y. Zhang, Automatic design of conformal cooling circuits for rapid tooling, Comput. Des. 43 (2011) 1001–1010, https://doi.org/10.1016/j.cad.2011.04.011.

[12] H. Park, X. Dang, Development of a smart plastic injection mold with conformal cooling channels, Procedia Manuf. 10 (2017) 48–59, https://doi.org/10.1016/j.promfg.2017.07.020.

[13] G.R. Berger, D. Zorn, W. Friesenbichler, F. Bevc, C.J. Bodor, Efficient cooling of hot spots in injection molding. A biomimetic cooling channel versus a heat-conductive mold material and a heat conductive plastics, Polym. Eng. Sci. 59 (2019) E180–E188, https://doi.org/10.1002/pen.25024.

[14] K.M. Au, K.M. Yu, Conformal cooling channel design and CAE simulation for rapid blow mould, Int. J. Adv. Manuf. Technol. 66 (2013) 311–324, https://doi.org/10.1007/s00170-012-4326-6.

[15] A.J. Norwood, P.M. Dickens, R.C. Soar, R. Harris, G. Gibbons, R. Hansell, Analysis of cooling channels performance, Int. J. Comput. Integr. Manuf. 17 (2004) 669–678, https://doi.org/10.1080/0951192042000237528.

[16] R. Hölker, A. Jäger, N. Ben Khalifa, A.E. Tekkaya, Controlling heat balance in hot aluminum extrusion by additive manufactured extrusion dies with conformal cooling channels, Int. J. Precis. Eng. Manuf. 14 (2013) 1487–1493, https://doi.org/10.1007/s12541-013-0200-1.

[17] C.C. Kuo, B.C. Chen, Development of hot embossing stamps with conformal cooling channels for microreplication, Int. J. Adv. Manuf. Technol. 88 (2017) 2603–2608, https://doi.org/10.1007/s00170-016-8970-0.

[18] W.S. Lim, H.S. Choi, S.Y. Ahn, B.M. Kim, Cooling channel design of hot stamping tools for uniform high-strength components in hot stamping process, Int. J. Adv. Manuf. Technol. 70 (2014) 1189–1203, https://doi.org/10.1007/s00170-013-5331-0.

[19] T.G. Spears, S.A. Gold, In-process sensing in selective laser melting (SLM) additive manufacturing, Integr. Mater. Manuf. Innov. 5 (2016) 16–40, https://doi.org/10.1186/s40192-016-0045-4.

[20] C. Liu, Z. Cai, Y. Dai, N. Huang, F. Xu, C. Lao, Experimental comparison of the flow rate and cooling performance of internal cooling channels fabricated via selective laser melting and conventional drilling process, Int. J. Adv. Manuf. Technol. 96 (2018) 2757–2767, https://doi.org/10.1007/s00170-018-1799-y.

[21] A.M. Kamat, Y. Pei, An analytical method to predict and compensate for residual stress-induced deformation in overhanging regions of internal channels fabricated using powder bed fusion, Addit. Manuf. 29 (2019) 100796, https://doi.org/10.1016/j.addma.2019.100796.

[22] D. Wang, Y. Wang, Y. Yang, J. Lu, Z. Xu, S. Li, K. Lin, D. Zhang, Research on design optimization and manufacturing of coating pipes for automobile seal based on selective laser melting, J. Mater. Process. Technol. 273 (2019) 116227, https://doi.org/10.1016/j.jmatprotec.2019.05.008.

[23] J.C. Snyder, C.K. Stimpson, K.A. Thole, D. Mongillo, Build direction effects on additively manufactured channels, J. Turbomach. 138 (2016), 051006, https://doi.org/10.1115/1.4032168.

[24] S. Siddique, M. Imran, M. Rauer, M. Kaloudis, E. Wycisk, C. Emmelmann, F. Walther, Computed tomography for characterization of fatigue performance of selective laser melted parts, Mater. Des. 83 (2015) 661–669, https://doi.org/10.1016/j.matdes.2015.06.063.

[25] J. Fay, Introduction to Fluid Mechanics, MIT Press, 1995.

[26] X. Xu, E. Sachs, S. Allen, M. Cima, Designing conformal cooling channels for tooling, Solid Freeform Fabr. Symp. Proc. (1998) 131–146.

[27] P. Wei, Z. Wei, Z. Chen, J. Du, Y. He, J. Li, Y. Zhou, The AlSi10Mg samples produced by selective laser melting: single track, densification, microstructure and mechanical behavior, Appl. Surf. Sci. 408 (2017) 38–50, https://doi.org/10.1016/j.apsusc.2017.02.215.

[28] F. Liu, X. Lin, C. Huang, M. Song, G. Yang, J. Chen, W. Huang, The effect of laser scanning path on microstructures and mechanical properties of laser solid formed nickel-base superalloy Inconel 718, J. Alloys. Compd. 509 (2011) 4505–4509, https://doi.org/10.1016/j.jallcom.2010.11.176.

[29] B. AlMangour, D. Grzesiak, J.-M. Yang, Scanning strategies for texture and anisotropy tailoring during selective laser melting of TiC/316L stainless steel nanocomposites, J. Alloys. Compd. 728 (2017) 424–435, https://doi.org/10.1016/j.jallcom.2017.08.022.

[30] F. Geiger, K. Kunze, T. Etter, Tailoring the texture of IN738LC processed by selective laser melting (SLM) by specific scanning strategies, Mater. Sci. Eng. A 661 (2016) 240–246, https://doi.org/10.1016/j.msea.2016.03.036.

[31] I. Yadroitsev, I. Smurov, Surface morphology in selective laser melting of metal powders, Phys. Procedia 12 (2011) 264–270, https://doi.org/10.1016/j.phpro.2011.03.034.

powder, Appl. Surf. Sci. 254 (2007) 980–983, https://doi.org/10.1016/j.apsusc.2007.08.046.

[32] L. Thijs, F. Verhaeghe, T. Craeghs, J. Van Humbeeck, J.P. Kruth, A study of the microstructural evolution during selective laser melting of Ti-6Al-4V, Acta Mater. 58 (2010) 3303–3312, https://doi.org/10.1016/j.actamat.2010.02.004.

[33] L. Chin, L.E. Ehrlich, M.J. Powell-palm, C. Montgomery, J. Beuth, J.A. Malen, Thermal conductivity of metal powders for powder bed additive manufacturing, Addit. Manuf. 21 (2018) 201–208, https://doi.org/10.1016/j.addma.2018.02.002.

[34] S. Safdar, A.J. Pinkerton, L. Li, M.A. Sheikh, P.J. Withers, An anisotropic enhanced thermal conductivity approach for modelling laser melt pools for Ni-base super alloys, Appl. Math. Model. 37 (2013) 1187–1195, https://doi.org/10.1016/j.apm.2012.03.028.

[35] A.M. Kamara, W. Wang, S. Marimuthu, L. Li, Modelling of the melt pool geometry in the laser deposition of nickel alloys using the anisotropic enhanced thermal conductivity approach, Proc. Inst. Mech. Eng. Part B J. Eng. Manuf. 225 (2011) 87–99, https://doi.org/10.1177/09544054JEM2129.

[36] C. Kamath, B. El-Dasher, G.F. Gallegos, W.E. King, A. Sisto, Density of additively-manufactured, 316L SS parts using laser powder-bed fusion at powers up to 400 W, Int. J. Adv. Manuf. Technol. 74 (2014) 65–78, https://doi.org/10.1007/s00170-014-5954-9.

[37] S. Feng, R. Zhang, C. Huang, J. Wang, Z. Jia, J. Wang, An investigation of recast behavior in laser ablation of 4H-silicon carbide wafer, Mater. Sci. Semicond. Process. 105 (2020) 104701, https://doi.org/10.1016/j.mssp.2019.104701.

[38] B. Cheng, K. Chou, Thermal stresses associated with part overhang geometry in electron beam additive manufacturing: process parameter effects, Proc. Annu. Int. Solid Free. Fabr. Symp. (2014) 1076–1087.

[39] A. Bin Anwar, Q.C. Pham, Selective laser melting of AlSi10Mg: effects of scan direction, part placement and inert gas flow velocity on tensile strength, J. Mater. Process. Technol. 240 (2017) 388–396, https://doi.org/10.1016/j.jmatprotec.2016.10.015.

[40] B. Ferrar, L. Mullen, E. Jones, R. Stamp, C.J. Sutcliffe, Gas flow effects on selective laser melting (SLM) manufacturing performance, J. Mater. Process. Technol. 212 (2012) 355–364, https://doi.org/10.1016/j.jmatprotec.2011.09.020.

[41] C.J. Kong, C.J. Tuck, I.A. Ashcroft, R.D. Wildman, R. Hague, High density TI6AL4V via SLM processing: microstructure and mechanical properties, 22nd Annu. Int. Solid Free. Fabr. Symp. - An Addit. Manuf. Conf. SFF 2011 (2011) 475–483.

[42] A. Charles, A. Elkaseer, L. Thijs, S.G. Scholz, Dimensional errors due to overhanging features in laser powder bed fusion parts made of Ti-6Al-4V, Appl. Sci. 10 (2020) 2416, https://doi.org/10.3390/app10072416.